MNRAS 000, 1–?? (2022) Preprint 29 August 2022 Compiled using MNRAS LATEX style file v3.0

Finite-temperature effects in dynamical spacetime binary neutron star merger simulations: Validation of the parametric approach

Carolyn A. Raithel,[1,2,3]⋆ Pedro Espino,[4,5] Vasileios Paschalidis,[6,7]
[1] School of Natural Sciences, Institute for Advanced Study, Princeton, NJ 08540, USA
[2] Princeton Center for Theoretical Science, Princeton University, Princeton, NJ 08540, USA
[3] Princeton Gravity Initiative, Princeton University, Princeton, NJ 08540, USA
[4] University of California Berkeley Department of Physics, Berkeley, CA 94720, USA
[5] Institute for Gravitation and the Cosmos, The Pennsylvania State University, University Park, PA 16802, USA
[6] Department of Astronomy and Steward Observatory, University of Arizona, Tucson, Arizona 85721, USA
[7] Department of Physics, University of Arizona, Tucson, Arizona 85721, USA

arXiv:2206.14838v2 [astro-ph.HE] 25 Aug 2022

Accepted XXX. Received YYY; in original form ZZZ

ABSTRACT

Parametric equations of state (EoSs) provide an important tool for systematically studying EoS effects in neutron star merger simulations. In this work, we perform a numerical validation of the M^*-framework for parametrically calculating finite-temperature EoS tables. The framework, introduced in Raithel et al. (2019), provides a model for generically extending any cold, β-equilibrium EoS to finite-temperatures and arbitrary electron fractions. In this work, we perform numerical evolutions of a binary neutron star merger with the SFHo finite-temperature EoS, as well as with the M^*-approximation of this same EoS, where the approximation uses the zero-temperature, β-equilibrium slice of SFHo and replaces the finite-temperature and composition-dependent parts with the M^*-model. We find that the approximate version of the EoS is able to accurately recreate the temperature and thermal pressure profiles of the binary neutron star remnant, when compared to the results found using the full version of SFHo. We additionally find that the merger dynamics and gravitational wave signals agree well between both cases, with differences of $\lesssim 1-2\%$ introduced into the post-merger gravitational wave peak frequencies by the approximations of the EoS. We conclude the M^*-framework can be reliably used to probe neutron star merger properties in numerical simulations.

Key words: stars: neutron – (transients:) neutron star mergers – equation of state – methods: numerical

1 INTRODUCTION

Binary neutron star mergers provide a promising new avenue for studying the dense-matter equation of state (EoS) across a wide range of conditions. During the early inspiral, the neutron stars are thermodynamically cold and the interior matter remains in β-equilibrium. As the neutron stars come into contact with one another, shock heating raises the temperature of the system to $\mathcal{O}(10)$s of MeV (e.g., Baiotti & Rezzolla 2017; Paschalidis & Stergioulas 2017, for reviews), at which point the thermal pressure is significant and can influence the evolution of the post-merger remnant (Oechslin et al. 2007; Baiotti et al. 2008; Bauswein et al. 2010b,a; Sekiguchi et al. 2011; Paschalidis et al. 2012; Raithel et al. 2021a). At these temperatures, the matter can also deviate significantly from equilibrium (e.g., Rosswog & Liebendoerfer 2003; Sekiguchi et al. 2011; Hammond et al. 2021; Most & Raithel 2021), and out-of-equilibrium effects may become important for some EoSs (e.g., Most et al. 2022). If the remnant object avoids prompt collapse to a black hole, the massive neutron star remnant will additionally probe matter at extreme densities and masses not accessible by isolated neutron stars. Such conditions provide a unique laboratory for studying the dense-matter EoS.

When it comes to exploring realistic EoS effects in neutron star merger simulations, there are two main approaches. The first is to use a tabulated, finite-temperature EoS, which can be calculated with a variety of methods, ranging from the liquid-drop model of Lattimer & Swesty (1991), to the relativistic mean-field (RMF) approach of Shen et al. (1998). Another ten models have been computed with the statistical model of Hempel et al. (2012) for different RMF models and nuclear mass tables, while many more finite-temperature EoSs are being added to the available libraries, thanks in part to the CompOSE database which enables public sharing of such tables (Typel et al. 2015). These microphysical EoS tables provide a robust method for testing the predictions of a particular theory with a given set of nuclear parameters, coupling constants, and calculation methods. For a review of finite-temperature EoSs, see Oertel et al. (2017).

⋆ E-mail: craithel@ias.edu

© 2022 The Authors

However, for general comparisons of neutron star merger properties, there are some drawbacks to limiting our studies to the existing sample of tables. For example, the existing catalog of finite-temperature EoS tables currently includes few models that predict neutron stars with radii $\lesssim 12$ km, whereas recent constraints from low-mass X-ray binary observations and from GW170817 provide significant evidence for more compact stars, with radii between ~ 11 and 13 km. (for reviews, see Özel & Freire 2016; Baiotti 2019; Raithel 2019; Chatziioannou 2020).

Additionally, when comparing simulation results that use existing finite-temperature EoS tables, there are multiple differences between the tables that complicate straightforward comparisons. For example, these tables vary not only in their predictions for the neutron star compactness or maximum mass, but they also differ in the thermal pressure that they predict at a given temperature (see Fig. 1 of Raithel et al. 2021a). While it is well understood that differences in the cold physics (affecting, e.g., the stellar compactness) can influence the post-merger evolution, differences in the finite-temperature part of the EoS can also influence post-merger properties such as the ejecta and the gravitational wave emission (Bauswein et al. 2010b; Figura et al. 2020; Raithel et al. 2021a). When using pre-existing EoS tables in simulations, it can be difficult to disentangle the effects of changing these properties simultaneously.

In order to get around these limitations, a second approach has been developed to study EoS effects in neutron star mergers more systematically. In this approach, a cold EoS is extended to finite-temperatures with an approximate prescription, which can be held fixed or varied, independently of the cold EoS. The cold EoS could be a microphysical EoS tabulated at zero-temperature, of which there are many more options than in the finite-temperature case (e.g., Özel & Freire 2016); or it could be an agnostic parametrization, such as piecewise polytropes (Read et al. 2009; Özel & Psaltis 2009), which can be designed to probe a new part of the parameter space. In early merger simulations, it was common to approximate the thermal extension of the EoS with a constant thermal index, according to $P_{\rm th} = \epsilon_{\rm th}(\Gamma_{\rm th}-1)$, where $P_{\rm th}$ and $\epsilon_{\rm th}$ are the thermal pressure and energy density, respectively, and $\Gamma_{\rm th}$ is a constant (Janka et al. 1993). For $\Gamma_{\rm th} = 5/3$, this so-called "hybrid approach" is equivalent to an ideal-fluid prescription. For more realistic EoSs, the thermal index is expected to vary significantly with the density, as the matter becomes degenerate (Constantinou et al. 2015).

In Raithel et al. (2019, 2021b) (hereafter RÖP), a new framework was developed for extending cold, β-equilibrium EoSs to finite-temperatures and arbitrary electron fractions. In that work, the high-density thermal prescription is based on a two-parameter approximation of the particle effective mass, in order to account for the effects of degeneracy on the thermal pressure at high-densities, and thus to provide a more realistic density-dependence for the effective thermal index. The framework of RÖP also allows for the initial EoS to be extended from β-equilibrium to arbitrary electron fractions, using a parametrization of the nuclear symmetry energy. In RÖP , it was shown that for a sample of nine published, finite-temperature EoS tables based on relativistic energy density functionals, the M^*-framework was able to re-create the pressure of the complete models with errors of $\lesssim$30%, at densities and temperatures of interest for neutron star mergers. The M^*-framework reduces the error of the thermal pressure model compared to the ideal-fluid based approximation of the hybrid approach by up to 3-4 orders of magnitude. The first successful numerical implementation of the M^*-framework and application to binary neutron star mergers was presented in Raithel et al. (2021a) (see also Raithel & Paschalidis 2022 where the implementation was added to different cold EoS parametrization frameworks).

In this paper, we provide a complementary validation of the M^*-framework, by demonstrating that the numerical simulation of a binary neutron star merger evolved with an M^*-approximated EoS can recreate the results that are found with the full version of the EoS. We do so using the finite-temperature EoS table SFHo (Steiner et al. 2013). In particular, we take the zero-temperature, β-equilibrium slice of SFHo, and extend it to finite-temperatures and arbitrary electron fractions using the M^*-framework; thereby replacing the finite-temperature and composition-dependent parts with the M^*-model at high densities. We perform evolutions of binary neutron star mergers with the full version of SFHo and with its M^* approximation, and we confirm that the M^*-approximation accurately recreates the results found with the full EoS.

We note that this comparison is purely a validation of the framework, rather than its intended use. That is, if one's goal is to use a particular, existing dense-matter model (such as SFHo), then the existing published table can and should be used. The advantage of the M^*-model is that it allows for new EoSs to be constructed in new parts of the parameter space. In this paper, we approximate SFHo with the simple goal of validating that the M^*-framework is able to recreate realistic merger evolutions. We focus in particular on diagnostics and observable properties that are sensitive to the high-density EoS, which is the regime the M^*-framework is designed to approximate (in contrast to the hybrid approach, which breaks down at high densities). To that end, we confirm that evolutions with the M^*-framework lead to realistic thermal profiles of the merger remnant, and that they reproduce the post-merger dynamics and gravitational wave emission predicted by an existing, tabulated EoS.

The outline of the paper is as follows. In Sec. 2, we summarize the construction of the approximate EoS table. In Sec. 3, we describe the numerical set-up for our simulations. We present the simulation results in Sec. 4. We discuss the implications of these findings and conclude in Sec. 5. Unless otherwise indicated, we use natural units in which $G = c = k_B = 1$.

2 PARAMETRIC MODELING OF THE FINITE-TEMPERATURE EOS

We start with a short overview of the construction of the approximate EoS table. We do not repeat all the details of the parametric model for the thermal and composition-correction terms. The complete framework can be found in Raithel et al. (2019, 2021b). Here, we focus in particular on the details of the construction that are most relevant for the comparison to an existing, tabulated EoS.

2.1 The SFHo EoS

We validate the M^*-framework against the SFHo EoS (Steiner et al. 2013), which was calculated within the statistical framework of Hempel & Schaffner-Bielich (2010) with a new set of relativistic mean field parameters designed to match neutron star observations. In particular, SFHo predicts the radius of a 1.4 $M_\odot$ neutron star to be 11.89 km and the maximum mass to be 2.06 $M_\odot$, making it among the softest finite-temperature EoSs that are currently available.

In addition to its compatibility with observational data, we also choose SFHo as it poses a stringent "stress test" for modeling finite-temperature effects in a merger. This is because stars that are very compact, like those predicted by SFHo, reach shorter separations before merging, leading to more violent collisions and, accordingly, a higher degree of shock heating (e.g., Bauswein et al. 2013). Additionally, for a soft EoS such as SFHo, because the overall cold pressure is relatively low, any thermal pressure contributes a greater fraction of the total pressure than would be the case for a stiffer EoS. Thus, by validating the M^*-framework with SFHo, we are testing a challenging part of the parameter space, where errors in the thermal framework should have the strongest impact on observable features. This allows us to place an upper bound on how the approximations of the M^*-framework might influence observable features, such as the gravitational wave signal.

2.2 Construction of 3D, approximate EoS tables

With this goal in mind, we construct the following test, which is summarized in Fig. 1. We start by extracting a 1D constant-temperature slice from the full table for SFHo, which we obtain from `stellarcollapse.org`. We label this process "Projection" in Fig. 1 and we choose the 1D slice to correspond to the EoS at approximately zero-temperature[1] and in β-equilibrium. We then extend the 1D slice of the EoS to finite-temperatures and arbitrary electron fraction using the complete M^*-framework.[2] In skeletal format, this extension is performed according to

$$P(n, T, Y_e) = P(n, T \approx 0, Y_e^\beta) + P_{\rm th}(n, T, Y_e) + P_{\rm sym}(n, Y_e) \quad (1)$$

where P is the pressure, n is the number density, T is the temperature, Y_e is the electron fraction, and Y_e^β is a short-hand notation to indicate the electron fraction for cold matter in β-equilibrium (we note that Y_e^β is in fact density-dependent, but we suppress this dependence for clarity). Thus, in Eq. (1), the first term is simply the cold, β-equilibrium EoS; the second term represents the thermal correction term; and the third term represents the composition-correction term, which extends the matter to non-equilibrium compositions.

[1] In practice, the lowest temperature reliably included in the published tables is $T = 0.1$ MeV. At this temperature, the thermal pressure is completely subdominant compared to the cold pressure, rendering thermal effects negligible. Thus, $T = 0.1$ MeV is a reasonable approximation of "cold" matter.

[2] We note that, throughout this work, we use the term the "M^*-framework" to refer to the complete model of RÖP , including both the finite-temperature *and* composition-dependent correction terms outlined in eq. (1).

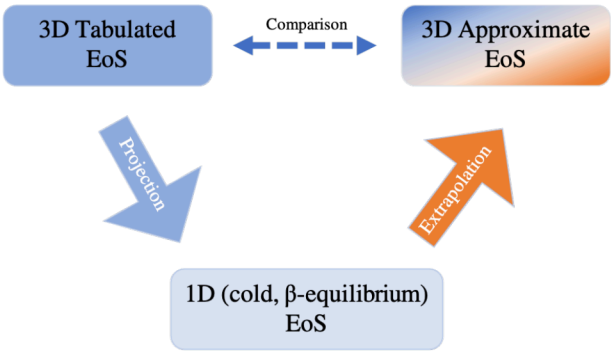

Figure 1. Cartoon schematic of the construction of the approximate 3D tables.

The RÖP model for the thermal pressure, $P_{\rm th}$, depends on two free parameters, n_0 and α, which govern the density-dependence of the particle effective mass function, $M^*(n)$. Here, we use the RÖP fit coefficients for SFHo, n_0 =0.22 fm^{-3} and α =0.89. [3]

The composition-correction term is constructed from a parametrization of the nuclear symmetry energy. The model for $P_{\rm sym}$ depends on the standard symmetry energy expansion parameters S_0 and L_0, which are related to the magnitude and slope of the symmetry energy at the nuclear saturation density; as well as a free parameter, γ, which extrapolates the symmetry energy model to higher densities. In constructing the approximate version of SFHo, we use the published SFHo values of S_0=31.57 MeV and L_0=47.10 MeV (Steiner et al. 2013), and the fit value of γ =0.41 provided in RÖP . For the complete expressions for $P_{\rm th}(n, T, Y_e)$ and $P_{\rm sym}(n, Y_e)$, as well as the corresponding expressions for the energy and the sound speed, see Raithel et al. (2019).

Finally, we note that the M^*-framework is designed to approximate thermal and composition-dependent effects in the high-density regime (i.e., above the nuclear saturation density, $n_{\rm sat}$ = 0.16 fm^{-3}). We do not attempt to use the M^*-model at very low densities where (1) the physics is well understood and there is no need for approximate models to explore new parts of the parameter space, and (2) the symmetry energy approximation is complicated by the emergence of nuclei, for which the assumption of homogenous nuclear matter no longer applies. For further discussion of the latter point and for the solution we adopt (which involves applying a power-law tail, to ensure the symmetry energy correction term goes smoothly to zero at low densities), see Appendix A in Most & Raithel (2021). For these reasons, we switch to the full version of the EoS table in the low density regime. The transition between the low-density EoS table and our high-density, approximate table is performed using the free-energy matching procedure of Schneider et al. (2017), which ensures that the merged EoS remains thermodynamically consistent. We perform this matching across a transition window from $n = 6.3 \times 10^{-5}$ to 0.08 fm^{-3}. This ensures that at densities

[3] These values correspond to the best-fit parameters characterizing $M^*(n)$ for symmetric nuclear matter ($Y_e = 0.5$), fit together at $T = 1, 10, 47.9$ MeV. The effective mass function for SFHo was provided via the website of M. Hempel (priv. communication). See RÖP for details.

above $0.5n_{\rm sat}$, we are exclusively using the approximate EoS model, but that at lower densities, the full table is smoothly approached.

In order to compare the approximate and full versions of the 3D EoS tables in a merger simulation, there is one final step required: the construction of the initial data. We describe this further in Sec. 3.2; but here, we note that this additionally requires the extraction of a 1D cold, β-equilibrium slice from the approximate 3D EoS table. This, in turn, requires providing chemical potentials in a way that is consistent with the rest of the M^*-approximation, in particular with the symmetry energy description. We calculate approximate chemical potentials for the approximate SFHo table following the procedure described in Appendix B of Most & Raithel (2021). A comparison of the resulting, approximate EoS with the full version of SFHo is presented in Appendix A.

3 NUMERICAL METHODS

In this section we highlight the numerical methods used to test our EoS framework. We include details on our extensions to the open-source `IllinoisGRMHD` code to allow for tabulated, finite-temperature EoS compatiblity. We also provide details on the initial conditions used for our simulations. Finally, we discuss the diagnostics used to compare and contrast the results of our simulations using the EoS tables described in Sec. 2.

3.1 Evolution code

Our evolution code consists of an updated version of the `IllinoisGRMHD` code (Etienne et al. 2015), which is described and validated in detail in Espino et al. (2022). `IllinoisGRMHD` solves the equations of general relativistic ideal magnetohydrodynamics (GRMHD) in a dynamical spacetime, within the Baumgarte-Shapiro-Shibata-Nakamura (BSSN) formulation (Nakamura et al. 1987; Shibata & Nakamura 1995; Baumgarte & Shapiro 1999) of the 3+1 Arnowitt-Deser-Misner (ADM) formalism. `IllinoisGRMHD` works with the spacetime metric

$$ds^2 = -\alpha^2 dt^2 + \gamma_{ij}(dx^i + \beta^i dt)(dx^j + \beta^j dt), \quad (2)$$

where α is the lapse, β^i is the shift, $\gamma_{\mu\nu} = g_{\mu\nu} + n_\mu n_\nu$ is the induced metric, and $n^\mu = (1/\alpha, \beta^i/\alpha)$ is the future-pointing unit vector orthogonal to each space-like hypersurface. Our updates to `IllinoisGRMHD` include the evolution of the electron fraction $Y_{\rm e}$ and the use of state-of-the-art conservative-to-primitive routines which are compatible with finite-temperature EoSs. Specifically, we supplement `IllinoisGRMHD` with the addition of the equation for $Y_{\rm e}$ advection, assuming conservation of charged lepton number,

$$\partial_t(\tilde{Y}_{\rm e}) + \partial_j(v^j \tilde{Y}_{\rm e}) = 0, \quad (3)$$

where $\tilde{Y}_{\rm e} \equiv \alpha Y_{\rm e}\sqrt{\gamma}\rho_{\rm b}u^0$, $\rho_{\rm b}$ is the rest mass density, γ is the determinant of the 3-metric, and u^0 is the temporal component of the fluid 4-velocity. We emphasize that, as we assume the conservation of *charged* lepton number, Eq. (3) only captures the advection of $Y_{\rm e}$. In the presence of neutrinos, we expect source terms to appear on the right-hand-side of Eq. (3), which can alter the evolution of $Y_{\rm e}$ (Radice et al. 2016b; Foucart et al. 2016; Most et al. 2019; Giacomazzo et al. 2020; Radice et al. 2022). We leave the investigation of neutrino transport effects, with the use of our approximate EOS tables, to future work. The conservative-to-primitive routines within the public version of `IllinoisGRMHD` assume a polytropic, barotropic form for the EoS. To allow for generic, finite-temperature EoSs, we have added the conservative-to-primitive inversion algorithm of Palenzuela et al. (2015) to `IllinoisGRMHD`. This algorithm was originally implemented in the open-source conservative-to-primitive driver code of Siegel et al. (2018), which we have adapted to the Cactus framework within which `IllinoisGRMHD` operates. The conservative-to-primitive algorithm of Palenzuela et al. (2015) as implemented in Siegel et al. (2018) provides a robust and efficient method for general conservative-to-primitive inversion when using tabulated, finite-temperature EoSs and has been used in several GRMHD codes (Most et al. 2019; Giacomazzo et al. 2020).

The convergence of the updated `IllinoisGRMHD` code with a similar tabulated EoS was recently studied in Espino et al. (2022), where it was shown that the code converges at the expected second order rate, and that the code's convergence properties are generally consistent with those of other open-source GRMHD codes. We also find merger dynamics which are consistent with other open-source GRMHD codes. Importantly, our code produces similar merger times and remnant thermal profiles to the `GRHydro` (Mosta et al. 2014), `Spritz` (Giacomazzo et al. 2020), and `WhiskyTHC` (Radice et al. 2014) codes for astrophysical systems relevant to the present work (i.e., BNS mergers with the use of finite-temperature EoS tables). We discuss the convergence properties of our code, and provide comparisons to the results produced by other codes in Espino et al. (2022); we refer the reader to that work for further details.

We evolve the spacetime using the `McLachlan` spacetime evolution code (Brown et al. 2009; Reisswig et al. 2011) within the `EinsteinToolkit` (Loffler et al. 2012), which solves the Einstein equations within the BSSN formulation of the ADM 3+1 formalism. We evolve using the "1+log" slicing condition for the lapse (Bona et al. 1995) and a "Gamma-driver" condition for the shift, with the shift coefficient set to $\nu = 0.75$ (Alcubierre et al. 2003). For time-integration, we use a fourth-order Runge-Kutta scheme with a Courant-Friedrichs-Lewy (CFL) factor of 0.5, provided by the `MoL` thorn within the `EinsteinToolkit`.

3.2 Initial conditions

We construct binary neutron star initial data using the `LORENE` libraries.[4] `LORENE` requires the use of cold, barotropic EoS tables corresponding to nuclear matter in neutrinoless β-equilibrium, such that the pressure $P_\beta = P_\beta(\rho_{\rm b})$. We extract such EoS slices from the 3D tables described in Sec. 2 as follows: at each value of $\rho_{\rm b}$ available in the table, we fix the temperature to $T_{\rm cold} = 0.1$ MeV and locate the table entry that corresponds to β-equilibrium, such that

$$\mu_{\rm n} - \mu_{\rm p} - \mu_{\rm e} = 0, \quad (4)$$

where $\mu_{\rm n,p,e}$ are the neutron, proton, and electron chemical potentials, respectively. At each value of $\rho_{\rm b}$ considered,

[4] https://lorene.obspm.fr/

Eq. (4) is satisfied for a unique value of $Y_e = Y_e^\beta$. This procedure allows us to extract barotropic tables corresponding to β-equilibrium, such that $P_\beta(\rho_b) = P(\rho_b, Y_e^\beta, T_{cold})$, where P corresponds to the pressure in the full 3D table.

We use the resulting cold, β-equilibrium slice of the approximate SFHo table in order to construct initial data for an irrotational, equal-mass binary neutron star system on a quasi-circular orbit. We use this initial data for both the simulation with the full SFHo EoS, and the simulation with the approximate SFHo EoS. That is, we launch both simulations from initial data that were constructed with the approximate version of the SFHo table. Because the approximate version of the EoS is designed to be identical to the full version of SFHo at zero-temperature (as shown schematically in Fig. 1), the initial conditions should, in principle, be identical for both evolutions. In practice, however, there are some small differences in the approximate chemical potentials, which lead to small differences in the extracted β-equilibrium slices. As a result, the cold, β-equilibrium EoSs differ slightly; but, as we show in Appendix A, the difference between the cold, β-equilibrium pressures for the approximate and full versions of SFHo is $\lesssim$1% at densities above half the nuclear saturation density. As a result, our choice to adopt identical initial data for both simulations has negligible impact on the evolutions, as we will demonstrate below.

The centers-of-mass of each binary component are initially separated by 45 km and each star has a baryonic mass of $M_b = 1.42\ M_\odot$ and a gravitational mass of $M = 1.26\ M_\odot$, where the gravitational mass is defined as the ADM mass of a static Tolman-Oppenheimer-Volkoff (TOV) (Tolman 1939; Oppenheimer & Volkoff 1939) star with the same baryonic mass. The total ADM mass of the system is $M_{ADM} = 2.59\ M_\odot$. The central value of the specific enthalpy for each star is $h \approx 0.2112$, and total system angular velocity and orbital frequency are $\Omega \approx 1741$ rad/s and $f \approx 277$ Hz, respectively.

For each binary evolution, we use seven spatial refinement levels, which are separated by a 2:1 refinement ratio. The resolution on the finest refinement level corresponds to a grid spacing of $\Delta x = 152$ m, which means there are ~ 128 points across the diameter of each initial neutron star.

3.3 Diagnostics

We use several diagnostics to assess the state of our simulations and to compare results between the full and approximate versions of the SFHo EoS. All codes used for diagnostics are available within the `EinsteinToolkit` suite of codes (Loffler et al. 2012); in the following we highlight specific thorns used for each diagnostic, where relevant.

We monitor global scalar variables, including the maximum of the rest mass density, $\rho_{b,\,max}$, and the minimum of the lapse, α_{min}, to monitor partial gravitational collapse during the merger. To visually assess thermal features of the merger, we consider 2D equatorial snapshots of fluid variables, including the ratio of the thermal to the cold fluid pressure, P_{th}/P_{cold}, as well as the temperature, T. We also consider density profiles of these variables, to understand in a deeper manner the differences in thermal properties between the two simulations.

We extract gravitational waves within the Newman-Penrose (NP) formalism (Newman & Penrose 1962; Penrose 1963), by calculating the NP scalar Ψ_4 which is decomposed into $s = -2$ spin-weighted spherical harmonics, with use of the `Multipole` thorn within the `EinsteinToolkit`. The coefficients of the decomposition are labeled as $\psi_4^{\ell,m}$. For the dominant $\ell = m = 2$ mode, we compute $|\psi_4^{2,2}(t)|$ at several extraction radii and report the value in the wave zone, and we use this to extract the polarizations of the GW strain h,

$$\Psi_4 = \ddot{h}_+ - i\ddot{h}_\times, \tag{5}$$

using the fixed-frequency integration method (Reisswig & Pollney 2011).

4 RESULTS

We now turn to the results of merger evolutions using the full and approximate SFHo tables. We start with an overview of the merger dynamics and remnant properties, and then discuss in detail the thermal properties of the remnant, in order to understand how the EoS modeling affects the post-merger evolution. Finally, we compare the gravitational wave emission for both evolutions, as this is a directly observable signal which is sensitive to the high-density EoS. For all diagnostics, we find strong agreement between the results found using the full and the approximate versions of the SFHo table.

4.1 Merger overview

We start with a short overview of the merger. For both evolutions, we track the final ∼6 orbits prior to merger. Throughout the inspiral, we find that the neutron stars remain stable and show no signs of significant heating. In both cases, the binaries have a time-to-merger of 17.2 ms, (where this time, t_{mer}, is defined as the time when the gravitational wave strain reaches a maximum; see Sec. 4.3). The time-to-merger is nearly identical for the two versions of the EoS, with only a 0.04 ms difference (0.2% fractional difference) in t_{mer}.

The rest mass of the merger remnant is $\sim 2.88\ M_\odot$ in both cases, which exceeds the maximum rest-mass of the zero-temperature Kepler sequence of $2.85\ M_\odot$ for this EoS. This suggests that the remnant is likely supported by a combination of differential rotation and thermal pressure (Paschalidis et al. 2012), but that it will eventually collapse. The timescales on which differential rotation is removed are significantly longer than our full evolution timescale (Paschalidis & Stergioulas 2017; Iosif & Stergioulas 2021); as such, we do not expect to find a black hole remnant during our simulations. Indeed, we find no signs of collapse by the end of our simulations, which last ∼20 ms past the merger. The top panel of Fig. 2 shows the minimum lapse function over the course of the evolution. It is approximately constant at late times, indicating that the remnant is indeed stable for both evolutions.

We additionally find strong agreement in the evolution of the maximum rest-mass density between the two EoSs, as shown in the bottom panel of Fig. 2. For both versions of the EoS, the maximum rest mass density at the end of the evolutions is 4.94 ρ_{sat}, with a fractional difference between the two cases of only 0.16%.

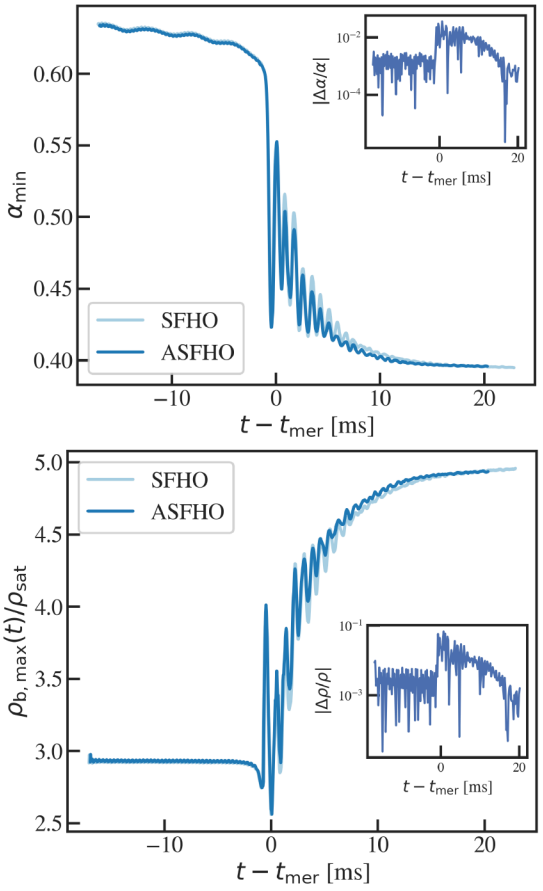

Figure 2. Top: Minimum lapse as a function of time for both evolutions. Bottom: Maximum rest mass density for the same evolutions, normalized to the nuclear saturation density. The results from the simulation using the full SFHo table are shown in light blue, while the results with the approximate SFHo table (labeled "ASFHO") are shown in dark blue. The insets show the fractional difference between the two cases.

4.2 Thermal properties of the remnant

The thermal profiles of the remnant are also very similar. We show equatorial snapshots of the thermal pressure, relative to the cold pressure, in Fig. 3. The results using the full SFHo table are shown in the top row, and those from the evolution with the approximate SFHo table are shown in the bottom row. The columns show snapshots at three times during and after merger.

From these snapshots, we find that the degree of heating during and after merger is qualitatively very similar for both the full and approximate SFHo evolutions. In both cases, we find that there is strong shock heating at the merger interface, which leads to substantial thermal pressure ($\gtrsim$ 10% of the cold pressure) in the outer layers of the stars. However, in the innermost core of the remnant, the thermal pressure remains subdominant to the cold pressure for both cases.

The corresponding temperatures for each snapshot are shown in Fig. 4. We find peak temperatures in excess of 50 MeV for both versions of the EoS. Additionally, we find that the temperature peaks away from the center of the remnant (as seen in the bright "ring" in the right columns of Fig. 4), which is a result of the particular M^*-parameters used here. In Raithel et al. (2021a), it was shown that the depth to which the shock-heating penetrates the remnant depends on the choice of M^*-parameters, with some choices of M^*-parameters leading to the appearance of a high-temperature "ring" and other choices leading to temperatures that peak closer to the center of the remnant. The similarity of the temperature ring features in Fig. 4 thus already starts to indicate that the thermal prescription in the M^*-version of the EoS provides a realiable approximation to that of the full SFHo table.

We explore these thermal profiles more quantitively in Fig. 5, where we show each quantity as a function of the density for the final snapshot ($t - t_{\rm mer} \sim$20 ms). In this figure, the markers represent values of a particular grid point in our simulations, while the lines represent the median of all values, calculated within density bins that are log-uniformly spaced. The density profiles of $P_{\rm th}/P_{\rm cold}$ are shown in the top panel of Fig. 5, while the temperature profiles are shown in the bottom panel.

We find that the thermal pressure profiles differ only slightly between the full and approximate versions of SFHo. In particular, for $\rho \approx 1 - 3\rho_{\rm sat}$, the difference in the median value of $P_{\rm th}/P_{\rm cold}$ is $\lesssim$ 5% between the two versions of the EoS. In both cases, we find that the thermal pressure is a significant fraction of the cold pressure, with $P_{\rm th} \gtrsim 0.1 P_{\rm cold}$ for densities below 3 $\rho_{\rm sat}$. Overall, this suggests a high degree of heating that extends to high densities within the star, and that the M^*-framework is able to accurately capture this response.

We likewise find close agreement in the temperatures reached in each simulation, with the approximate version of SFHo leading to slightly higher temperatures in the late-time remnant, but with a very similar density-dependence. In particular, Fig. 5 shows that the peak of the median temperature profile occurs at densities of $\sim 2\rho_{\rm sat}$ for both EoSs. For the evolution with the full version of SFHo, the median temperature profile in Fig. 5 peaks at a value of 42 MeV, whereas the median temperature profile for the evolution with the approximate EoS peaks at 45 MeV (fractional difference of 6%). In general, for $\rho < 3\rho_{\rm sat}$, we find that the median temperatures agree to within $\lesssim$10% between the two EoSs.

To place these differences in context, we can also consider the extent to which $P_{\rm th}/P_{\rm cold}$ and the temperature vary purely by changing the choice of M^*-parameters. In Raithel et al. (2021a), an extremal range of M^*-parameters was explored in a series of $1.4 + 1.4 M_\odot$ neutron star mergers, all governed by the same cold EoS (ENG). The choice of M^*-parameters was designed to bracket the range of uncertainty spanned by a sample of nine existing finite-temperature EoS tables. In that work, it was found that the median $P_{\rm th}/P_{\rm cold}$ can vary by a factor of a few shortly after merger, while the median temperature can vary by $\sim 2\times$, for the extreme set of M^*-parameters. Thus, when compared to the range of outcomes allowed by the degrees of freedom of the full M^*-model, the agreement between the full and approximate SFHo tables is very strong. We note one caveat when comparing to the results of Raithel et al. (2021a): namely, that the exact range of thermal outcomes depends not only on the M^*-parameters explored, but also on the cold EoS, as well as the binary mass and mass ratio of the merger. Additional parameter studies to quantify these dependencies will be the subject of future work.

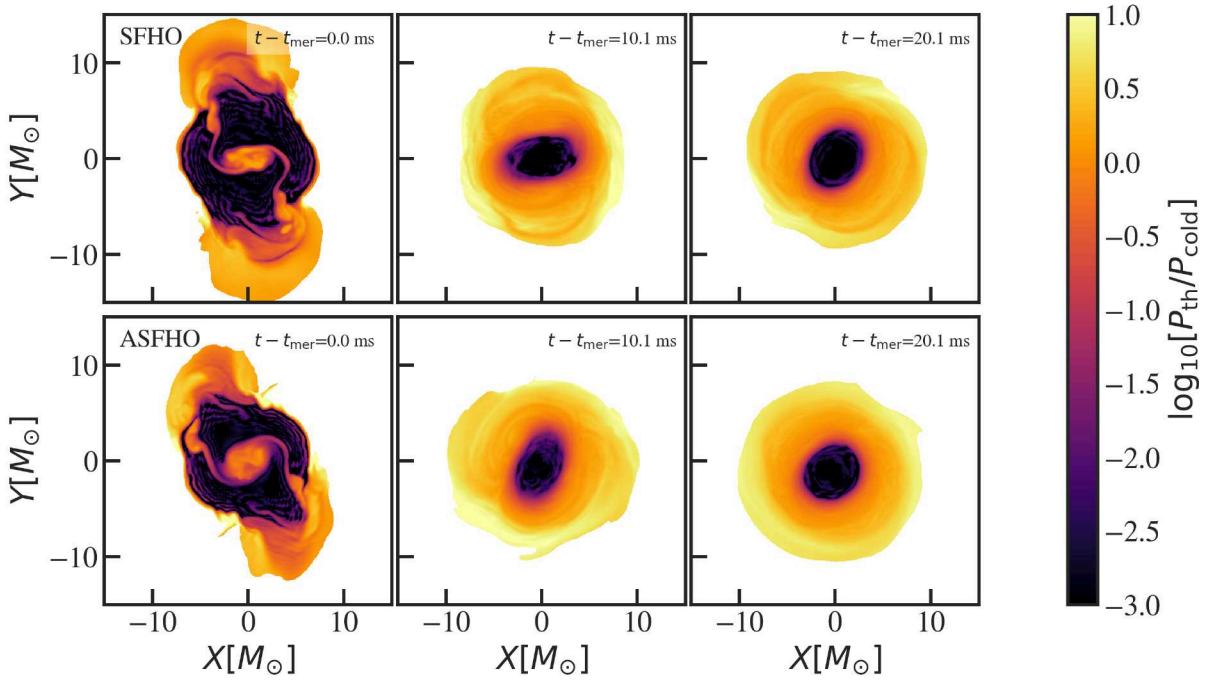

Figure 3. 2D equatorial snapshots of the thermal pressure relative to the cold pressure, at three times during and after the merger. The top row shows the results from the simulation run with the full SFHo table, while the bottom row corresponds to the results from the evolution with the approximate SFHo table, constructed using the M^*-framework. These figures include only matter with densities above $0.01\rho_{\rm b,max}(t = 0)$; matter at lower densities is masked in white. There is a slight difference in phase at merger due to the difference in initial conditions, but we find strong agreement in the degree of heating and the spatial distribution of $P_{\rm th}/P_{\rm cold}$ with the approximate model compared to the full table for SFHo.

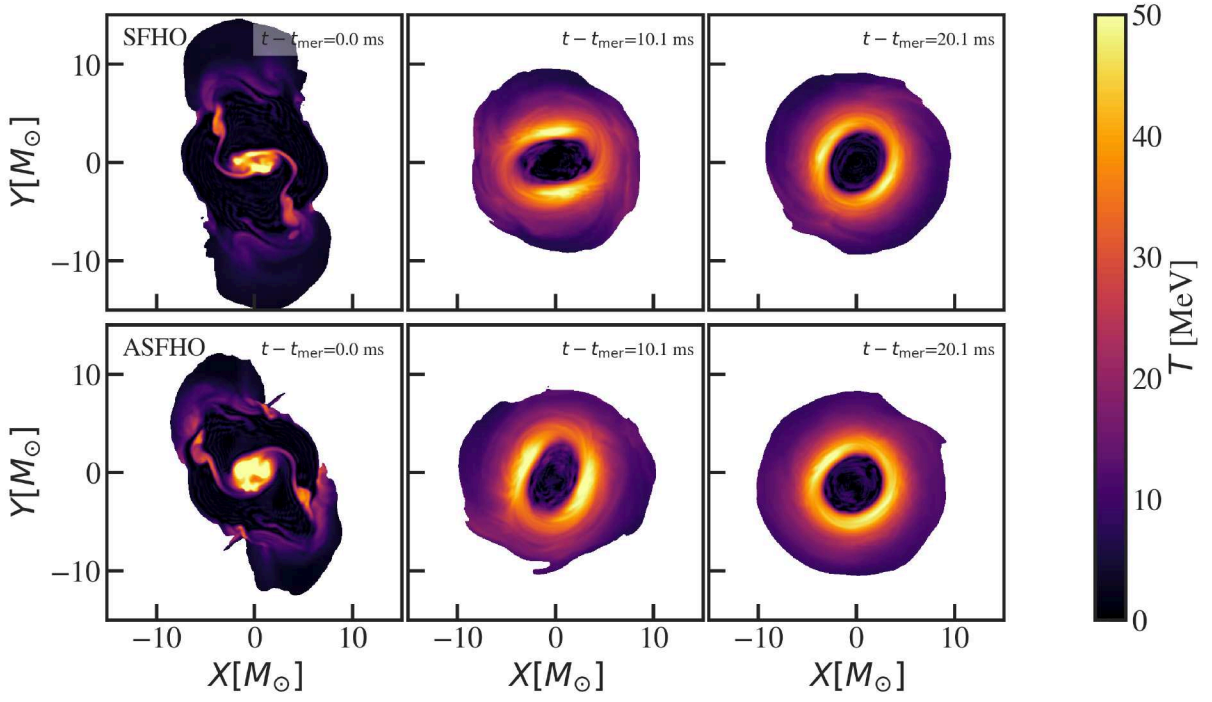

Figure 4. 2D equatorial snapshots of the temperature, at three times during and after the merger. The formatting of this figure is otherwise identical to Fig. 3.

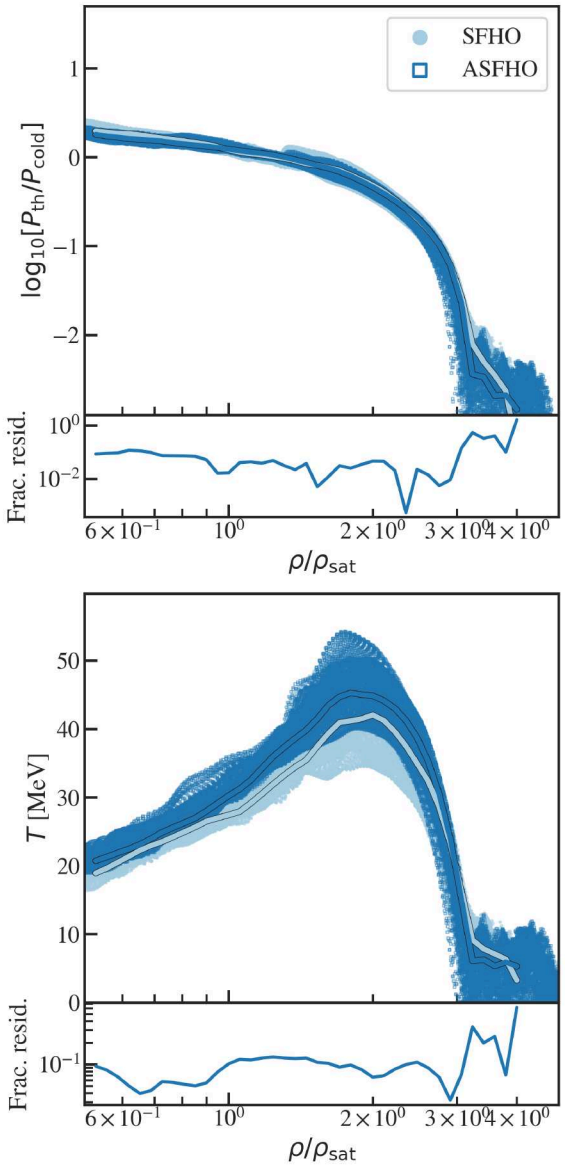

Figure 5. Late-time profiles of the thermal pressure and temperature as a function of the density. The points illustrate the spread of values found on the simulation grid, while the lines indicate the median value, calculated within density bins that are log-uniformly sampled. The lighter lines/points correspond to the results from the simulation with full SFHo table, while the darker lines/points correspond to the results from the approximate SFHo table ("ASFHO"). The lower panel to each figure shows the fractional residuals in the median values of $P_{\rm th}/P_{\rm cold}$ and the median temperature, respectively.

To summarize the results of this section: we find only small differences in the thermal pressure and temperature profiles when using the approximate version of the EoS. Moreover, we find that the qualitative shape and density-dependence of these profiles is accurately recreated with the M^*-framework.

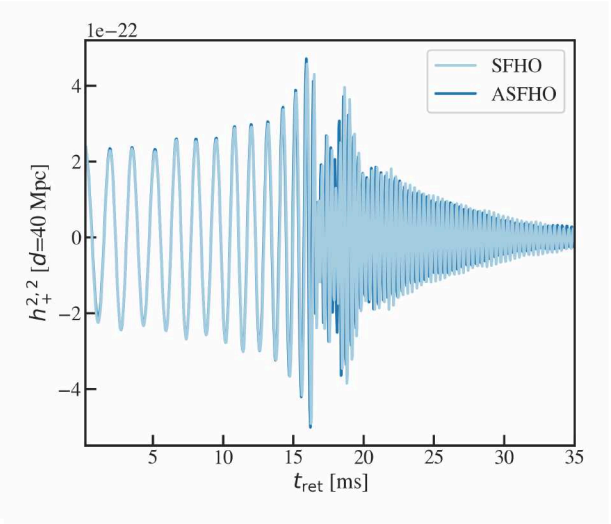

Figure 6. The $\ell = m = 2$ mode of the plus-polarized gravitational wave strain for a face-on merger located at a distance of 40 Mpc. The strain is plotted as a function of the retarded time, with the evolution using the full SFHo table shown in light blue, and the evolution using the approximate table shown in dark blue.

4.3 Gravitational wave signal

For the remainder of the paper, we turn now to the gravitational wave (GW) signal, as the key observable signature which is sensitive to the high-density part of the EoS. In Fig. 6, we show the $\ell = m = 2$ modes of the plus-polarized gravitational wave strain for each simulation, which have been computed as described in Sec. 3.3. This signal corresponds to a face-on merger located at 40 Mpc. We find that the inspiral portion of the GWs are nearly identical, as expected based on the fact that the zero-temperature, β-equilibrium slices of the EoSs are also nearly identical (to within $\lesssim$1% accuracy; see Appendix A) and the fact that the neutron stars remain thermodynamically cold ($P_{\rm th} \ll P_{\rm cold}$) during the inspiral.

In contrast, as discussed above, there is significant heating at and following merger, such that the pressure profile of the post-merger remnant has a substantial ($\gtrsim$ 10%) contribution from $P_{\rm th}$ at densities up to $3\rho_{\rm sat}$. Thus, if any differences were to arise between the GWs with the full and approximate versions of SFHo, we expect they would be most evident in the post-merger phase. Correctly modeling this phase of GW emission is of particular importance, as many studies have found empirical correlations between the oscillation frequencies of the post-merger remnant and properties of the neutron star EoS, such as the radius, stellar compactness, or tidal deformability (e.g., Bauswein et al. 2012; Bauswein & Janka 2012; Takami et al. 2014; Bernuzzi et al. 2015; Vretinaris et al. 2020; see also Raithel & Most 2022). In principle, such correlations make it possible to use a measurement of post-merger GWs to place immediate constraints on the neutron star EoS.

In order to explore these post-merger oscillation frequencies in more detail, we calculate the characteristic strain, $2f|\tilde{h}(f)|$, where f is the frequency and $\tilde{h}(f)$ is the Fourier transform of the strain. We compute this characteristic strain for the 20 ms signal immediately following the merger, using six overlap-

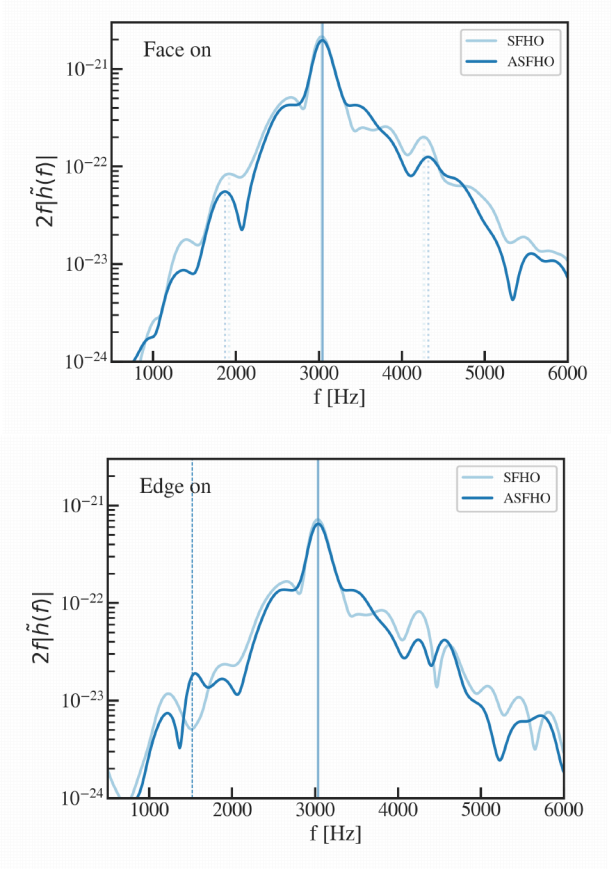

Figure 7. Characteristic strain of the post-merger gravitational wave signal. These spectra include all $\ell = 2, 3$ modes of the gravitational wave strain. The spectra for an optimally-oriented merger located at a distance of 40 Mpc are shown in the top panel, while the bottom panel shows the spectra for an edge-on orientation. The vertical lines indicate the location of the peak GW frequencies; the dotted lines (shown only for the face-on case) indicate the location of the secondary GW peak frequencies; and the dashed lines (shown only for the edge-on case) indicate the location of the $m = 1$ spectral peak.

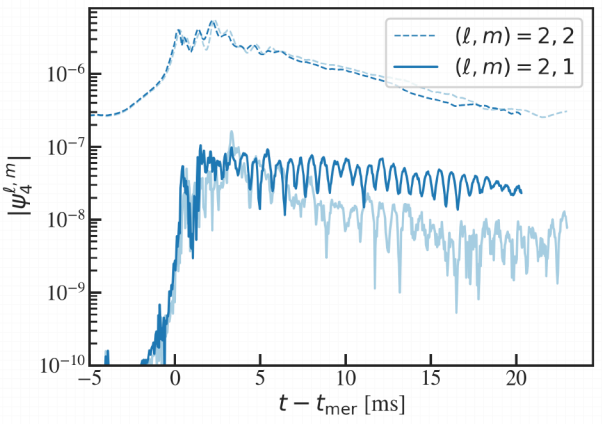

Figure 8. Amplitude of the Newman-Penrose scalar coefficients, after decomposition onto $s = -2$ spin-weighted spherical harmonics. The dashed lines show the $(\ell, m) = 2, 2$ mode of ψ_4, while the solid lines represent the $(\ell, m) = 2, 1$ mode. The color-coding is the same as the other figures in this paper, with the evolution using the full SFHo table shown in light blue, and the evolution using the approximate table shown in dark blue.

ping segments, which are windowed and padded as described in Appendix C of Most & Raithel (2021). We show the resulting spectra, including all $\ell = 2, 3$ modes of the strain, in Fig. 7. The top panel in this figure shows the spectra for an optimally-oriented (face-on) merger, while the bottom panel shows the spectra for an edge-on configuration. The solid vertical lines in these figures indicate the peak frequency of the gravitational waves, which we find to be 3.03 kHz for the evolution with the full version of the EoS, and 3.04 kHz for the evolution with the approximate version of SFHo. This difference of 12 Hz corresponds to a 0.4% fractional difference between the two cases. We additionally identify two secondary peaks, which are located equidistantly above and below the dominant peak, at ∼1.9 and 4.3 kHz. These are indicated with the dotted vertical lines in the top panel of Fig. 7, and agree between the full and approximate versions of the EoS with fractional differences of ∼1-2%. We note that the amplitude of these secondary peaks differ by ∼40%; however, the majority of the power is in the main spectral peak, where both EoSs lead to similar amplitudes, to within 9%.

In the edge-on version of the spectra, we find a small but interesting difference located at $f_{\rm peak}/2$, where $f_{\rm peak} \simeq 3$ kHz is the peak frequency. A feature at this location can indicate the formation and saturation of a one-arm, spiral instability in the remnant, which drives the production of $(\ell, m) = 2, 1$ gravitational waves (Paschalidis et al. 2015; East et al. 2016b,a; Lehner et al. 2016; Radice et al. 2016a). In Fig. 7, we find evidence of this $m = 1$ spectral peak only for the evolution that uses the approximate version of the EoS table, but we find no clear $m = 1$ peak in the evolution that uses the full SFHo table.

Interestingly, we find that the $m = 1$ mode does indeed develop and saturate for both versions of the EoS, but that it decays away slightly faster when the full version of the EoS table is used. This behavior is illustrated in Fig. 8, which shows the coefficients of $\psi_4^{\ell,m}$ over time for the dominant $(\ell, m) = 2, 2$ mode, as well as for the $(\ell, m) = 2, 1$ mode in question. We find the evolution of the dominant (2,2) mode is similar for both cases (consistent with the strains shown in Fig. 6), and that, in both cases, there is a similar growth of the $m = 1$ mode at merger. However, in the evolution with the approximate version of the SFHo table, the $m = 1$ mode stays saturated during the evolution, whereas it starts to decay approximately 5 ms after the merger when the full version of the SFHo table is used.

This subtle difference in the decay rate of $\psi_4^{2,1}$ suggests that the $m = 1$ mode may be somewhat more sensitive to the details of the thermal treatment, compared to the other spectral peaks discussed above. Nevertheless, we emphasize that this difference between the two evolutions is small and that, overall, we find strong agreement between the spectra near the dominant peak, which is expected to be the most easily observable feature for the near future.

In summary, these results confirm that simulations performed with the M^*-framework are able to accurately reproduce the dominant post-merger spectral frequencies found with the full SFHo EoS, with $\lesssim 1 - 2\%$ errors introduced by the approximations of the M^* model.

5 DISCUSSION AND CONCLUSIONS

In this work, we have performed a validation of the M^*-framework for calculating parametric, finite-temperature EoSs in the context of binary neutron star mergers. The framework, which was first introduced in Raithel et al. (2019), was shown in that work to recreate the pressure at finite-temperatures and arbitrary electron fractions with errors of $\lesssim 30\%$, for a sample of nine microphysical EoS tables. In this work, we choose one of these EoS tables, SFHo, for which we compare the outcomes of two full neutron star merger simulations, using either the full table or an approximate version, constructed with best-fit M^*-framework parameters. The SFHo EoS provides a challenging test case, as this is the softest of the original sample of nine EoSs. As a soft EoS, it predicts small neutron stars which are expected to collide with high impact energies, leading to significant shock heating. Additionally, due to the soft (i.e., relatively shallow) pressure profile of the cold EoS, errors in the thermal pressure will be dynamically more important than for the case of a stiffer cold EoS.

We have shown that the approximate version of SFHo, calculated with the M^*-framework, accurately captures the merger dynamics and remnant properties that are found with the full version of the EoS. In particular, we have compared the time-to-merger, rest mass of the remnant, and maximum rest-mass density of the remnant, all of which agree with the values found with the full EoS, with differences at the sub-percent level.

We have also investigated the thermal profiles of the remnant interior. We find very good agreement in the density-dependence and magnitude of $P_{\rm th}/P_{\rm cold}$ for the two EoSs. We likewise find good agreement in the temperature profiles, with the approximate version of SFHo leading to marginally higher temperatures in the late time remnant. Nevertheless, the median temperature in the late-time remnant ($t - t_{\rm mer} \sim 20$ ms) agrees for both versions of the EoS to within $\lesssim$10%, for $\rho < 3\rho_{\rm sat}$. We additionally find that the M^*-framework accurately captures the density-dependence of the temperature, with the temperature peaking at $2\rho_{\rm sat}$ in both cases, and decreasing at higher densities.

We place a particular emphasis on the gravitational wave signals predicted by the merger simulations, as these are an important ingredient for accurately interpreting upcoming observations. We find strong agreement in the inspiral gravitational wave strains, as expected based on the lack of significant heating prior to merger. The stricter test comes in the post-merger phase, when the thermal pressure exceeds 10% of the cold pressure (for $\rho < 3\rho_{\rm sat}$) and thus can be dynamically important in influencing the post-merger evolution. It is in this regime that errors in the M^*-approximations will be most evident. Even for the "stress test" of this soft EoS, we find only small differences in the post-merger gravitational wave strains. In particular, the peak frequencies of the characteristic strain agree identically, to within the frequency resolution of our spectra. The secondary peak frequencies also agree with the results from the full EoS, to within $1-2\%$.

We note that the M^*-framework was originally calibrated against a sample of EoSs that were calculated using relativistic energy density functionals, for which the model performed very well (e.g., errors of $\lesssim 15\%$ in the $T = 10$ MeV thermal pressure above nuclear densities; Raithel et al. 2019, 2021b). One natural question, then, is how general the framework and the associated validation presented in this work may be. In Raithel et al. (2019), the model was also compared against two non-relativistic Skyrme energy functionals, as well as a two-loop model, which is an extension of mean field theory. It was shown that the M^*-model had larger errors when compared against these non-RMF EoSs, but that the M^*-model still offered a significant improvement over the hybrid approach for a range of densities and temperatures. Recently, it was shown that the M^*-framework also performs very well when compared against calculations using nuclear many-body theory, with errors in pressure of $\lesssim 6\%$ at supranuclear densities (Tonetto & Benhar 2022). In contrast, recent results from chiral effective field theory have shown that repulsive three-body interactions can cause the effective mass function to start to rise at supranuclear densities (Carbone & Schwenk 2019; Keller et al. 2021), which will modify the density-dependence of the thermal pressure, and the effect of which is not included in the current M^*-model. We anticipate that the impact of this modified density-dependence for M^* would be smaller than, say, adopting a constant thermal index (as has been explored e.g., in Bauswein et al. 2010b; Figura et al. 2020; Raithel et al. 2021a), but this would be interesting to explore in future work.

In summary, we find that the merger dynamics, remnant properties, and gravitational waves found with the M^*-framework closely recreate the results found with the full version of the SFHo EoS. This provides a strong numerical validation of the M^*-framework, complementary to the analytic validation of the model reported in RÖP . More generally, these results confirm that the ($\lesssim$30%) errors introduced into the analytic EoS by the approximations of the M^*-framework do not significantly affect binary neutron star merger outcomes. Rather, these errors lead to minor (typically percent or sub-percent) differences in the merger outcomes, for best-fit M^* parameters.

Of course, when exploring a new part of the EoS parameter space, the best-fit model parameters are not known a priori. These must be bounded, either by experiment, theory, or by fits to existing samples of realistic EoSs. Understanding how the uncertainties in these parameters affect the merger properties requires systematic parameter surveys. A first such study has already been performed in Raithel et al. (2021a), where the authors bounded the range of merger outcomes for an extremal set of M^*-parameters, combined with a single, cold EoS. In that work, it was shown that by varying the M^*-parameters across an extremal range, the thermal pressure and temperature can vary significantly after merger. In comparison, the $\lesssim$5-10% deviations in thermal profiles that we find in this work between the the full and approximate SFHo tables are much smaller than the range of outcomes allowed by freely varying the M^*-parameters. While it may be possible to further improve this level of agreement by finely-tuning the M^*-parameters, that is not the goal of this study. Rather, this study aims to address whether the general functional form of the thermal framework, parametrized at the level of the effective mass function, can recreate realistic merger outcomes for an optimal set of parameters. The fact that the approximate and full tables agree so well – especially when compared to the range of outcomes allowed by the degrees of freedom of the M^*-model – provides strong validation of the approach. Additional parameter surveys to expand on the

results of Raithel et al. (2021a) will be the subject of future work.

In the meantime, the present study confirms that the M^*-framework can be reliably used to probe neutron star merger properties in numerical simulations in full general relativity.

ACKNOWLEDGEMENTS

CR would like to thank Elias Most for insightful discussions related to this work. CR gratefully acknowledges support from a joint postdoctoral fellowship at the Princeton Center for Theoretical Science, the Princeton Gravity Initiative, and as a John N. Bahcall Fellow at the Institute for Advanced Study. PE acknowledges support from NSF Grant PHY-2020275 (Network for Neutrinos, Nuclear Astrophysics, and Symmetries (N3AS)). This work was in part supported by NSF Grant PHY-1912619 and PHY-2145421 to the University of Arizona. The simulations presented in this work were carried out with the `Stampede2` cluster at the Texas Advanced Computing Center and the `Expanse` cluster at San Diego Supercomputer Center, under XSEDE allocation PHY190020. The simulations were also performed, in part, with the Princeton Research Computing resources at Princeton University, which is a consortium of groups led by the Princeton Institute for Computational Science and Engineering (PIC-SciE) and Office of Information Technology's Research Computing.

DATA AVAILABILITY

The data underlying this article will be shared on reasonable request to the corresponding author.

REFERENCES

Alcubierre M., Bruegmann B., Diener P., Koppitz M., Pollney D., Seidel E., Takahashi R., 2003, Phys. Rev., D67, 084023
Baiotti L., 2019, Progress in Particle and Nuclear Physics, 109, 103714
Baiotti L., Rezzolla L., 2017, Reports on Progress in Physics, 80, 096901
Baiotti L., Giacomazzo B., Rezzolla L., 2008, Phys. Rev. D, 78, 084033
Baumgarte T. W., Shapiro S. L., 1999, Phys. Rev. D, 59, 024007
Bauswein A., Janka H.-T., 2012, Physical Review Letters, 108, 011101
Bauswein A., Oechslin R., Janka H. T., 2010a, Phys. Rev. D, 81, 024012
Bauswein A., Janka H.-T., Oechslin R., 2010b, Phys. Rev. D, 82, 084043
Bauswein A., Janka H.-T., Hebeler K., Schwenk A., 2012, Phys. Rev. D, 86, 063001
Bauswein A., Goriely S., Janka H. T., 2013, ApJ, 773, 78
Bernuzzi S., Dietrich T., Nagar A., 2015, Phys. Rev. Lett., 115, 091101
Bona C., Masso J., Seidel E., Stela J., 1995, Phys. Rev. Lett., 75, 600
Brown J. D., Diener P., Sarbach O., Schnetter E., Tiglio M., 2009, Phys. Rev. D, 79, 044023
Carbone A., Schwenk A., 2019, Phys. Rev. C, 100, 025805
Chatziioannou K., 2020, General Relativity and Gravitation, 52, 109
Constantinou C., Muccioli B., Prakash M., Lattimer J. M., 2015, Phys. Rev. C, 92, 025801
East W. E., Paschalidis V., Pretorius F., 2016a, Class. Quant. Grav., 33, 244004
East W. E., Paschalidis V., Pretorius F., Shapiro S. L., 2016b, Phys. Rev. D, 93, 024011
Espino P., Bozzola G., Paschalidis V., 2022, In preparation
Etienne Z. B., Paschalidis V., Haas R., Mösta P., Shapiro S. L., 2015, Classical and Quantum Gravity, 32, 175009
Figura A., Lu J.-J., Burgio G. F., Li Z.-H., Schulze H. J., 2020, Phys. Rev. D, 102, 043006
Foucart F., O'Connor E., Roberts L., Kidder L. E., Pfeiffer H. P., Scheel M. A., 2016, Phys. Rev. D, 94, 123016
Giacomazzo B., Cipolletta F., Kalinani J., Ciolfi R., Sala L., Giudici B., Giangrandi E., 2020, The Spritz Code, doi:10.5281/zenodo.3689751
Hammond P., Hawke I., Andersson N., 2021, Phys. Rev. D, 104, 103006
Hempel M., Schaffner-Bielich J., 2010, Nuclear Physics A, 837, 210
Hempel M., Fischer T., Schaffner-Bielich J., Liebendörfer M., 2012, ApJ, 748, 70
Iosif P., Stergioulas N., 2021, MNRAS, 503, 850
Janka H.-T., Zwerger T., Moenchmeyer R., 1993, A&A, 268, 360
Keller J., Wellenhofer C., Hebeler K., Schwenk A., 2021, Phys. Rev. C, 103, 055806
Lattimer J. M., Swesty D. F., 1991, Nuclear Physics A, 535, 331
Lehner L., Liebling S. L., Palenzuela C., Motl P. M., 2016, Phys. Rev. D, 94, 043003
Loffler F., et al., 2012, Classical and Quantum Gravity, 29, 115001
Most E. R., Raithel C. A., 2021, arXiv e-prints, p. arXiv:2107.06804
Most E. R., Papenfort L. J., Rezzolla L., 2019, MNRAS, 490, 3588
Most E. R., et al., 2022, MNRAS, 509, 1096
Mosta P., et al., 2014, Classical and Quantum Gravity, 31, 015005
Nakamura T., Oohara K., Kojima Y., 1987, Prog. Theor. Phys. Suppl., 90, 1
Newman E., Penrose R., 1962, J. Math. Phys., 3, 566
Oechslin R., Janka H.-T., Marek A., 2007, A&A, 467, 395
Oertel M., Hempel M., Klähn T., Typel S., 2017, Reviews of Modern Physics, 89, 015007
Oppenheimer J. R., Volkoff G. M., 1939, Physical Review, 55, 374
Özel F., Freire P., 2016, ARA&A, 54, 401
Özel F., Psaltis D., 2009, Phys. Rev. D, 80, 103003
Palenzuela C., Liebling S. L., Neilsen D., Lehner L., Caballero O., O?Connor E., Anderson M., 2015, Physical Review D, 92
Paschalidis V., Stergioulas N., 2017, Living Reviews in Relativity, 20, 7
Paschalidis V., Etienne Z. B., Shapiro S. L., 2012, Phys. Rev. D, 86, 064032
Paschalidis V., East W. E., Pretorius F., Shapiro S. L., 2015, Phys. Rev. D, 92, 121502
Penrose R., 1963, Phys. Rev. Lett., 10, 66
Radice D., Rezzolla L., Galeazzi F., 2014, Classical and Quantum Gravity, 31, 075012
Radice D., Bernuzzi S., Ott C. D., 2016a, Phys. Rev. D, 94, 064011
Radice D., Galeazzi F., Lippuner J., Roberts L. F., Ott C. D., Rezzolla L., 2016b, Mon. Not. Roy. Astron. Soc., 460, 3255
Radice D., Bernuzzi S., Perego A., Haas R., 2022, Mon. Not. Roy. Astron. Soc., 512, 1499
Raithel C. A., 2019, European Physical Journal A, 55, 80
Raithel C. A., Most E. R., 2022, arXiv e-prints, p. arXiv:2201.03594
Raithel C. A., Paschalidis V., 2022
Raithel C. A., Özel F., Psaltis D., 2019, ApJ, 875, 12
Raithel C. A., Paschalidis V., Ã-zel F., 2021a, Phys. Rev. D, 104, 063016
Raithel C. A., Özel F., Psaltis D., 2021b, ApJ, 915, 73

Read J. S., Lackey B. D., Owen B. J., Friedman J. L., 2009, Phys. Rev. D, 79, 124032
Reisswig C., Pollney D., 2011, Classical and Quantum Gravity, 28, 195015
Reisswig C., Ott C. D., Sperhake U., Schnetter E., 2011, Physical Review D, 83
Rosswog S., Liebendoerfer M., 2003, Mon. Not. Roy. Astron. Soc., 342, 673
Schneider A. S., Roberts L. F., Ott C. D., 2017, Phys. Rev. C, 96, 065802
Sekiguchi Y., Kiuchi K., Kyutoku K., Shibata M., 2011, Physical Review Letters, 107, 051102
Shen H., Toki H., Oyamatsu K., Sumiyoshi K., 1998, Nuclear Physics A, 637, 435
Shibata M., Nakamura T., 1995, Phys. Rev. D, 52, 5428
Siegel D. M., Mosta P., Desai D., Wu S., 2018, Astrophys. J., 859, 71
Steiner A. W., Lattimer J. M., Brown E. F., 2013, ApJ, 765, L5
Takami K., Rezzolla L., Baiotti L., 2014, Physical Review Letters, 113, 091104
Tolman R. C., 1939, Physical Review, 55, 364
Tonetto L., Benhar O., 2022
Typel S., Oertel M., Klähn T., 2015, Physics of Particles and Nuclei, 46, 633
Vretinaris S., Stergioulas N., Bauswein A., 2020, Phys. Rev. D, 101, 084039

APPENDIX A: COMPARISON OF PRESSURE APPROXIMATIONS

In this appendix, we present a brief comparison of the pressure approximation for SFHo. A more detailed exploration of the errors introduced by the M^*-framework at finite-temperatures and arbitrary electrons can be found in RÖP , for a larger sample of EoSs which includes SFHo.

Figure A1 shows the cold, β-equilibrium slices of the approximate and full versions of SFHo, along with the corresponding mass-radius and mass-tidal deformability curves. Although the approximate EoS table is constructed starting from the cold, β-equilibrium slice of the full EoS (see Fig. 1), the extrapolations to construct the 3D approximate table introduce some errors. As a result of small errors in the approximate chemical potentials, when we extract the β-equilibrium slice from the 3D approximate table, it does not exactly match the starting slice. This can be seen in the slight disagreement between the cold, β-equilibrium slices of the EoSs shown in Fig. A1. The error in the β-equilibrium slice is typically $\lesssim$1%, at densities above $0.1\rho_{\rm sat}$. Slightly larger errors (up to a few percent) can be found at lower densities, where the approximate EoS is being matched to the full table. The impact of these errors on the global properties of the neutron star (i.e., mass and radius) can be seen in the right panels of Fig. A1. The radius of a 1.4 $M_\odot$ neutron star differs by 0.03 km between the approximate and full EoS models (fractional difference of 0.3%), while the corresponding tidal deformabilities differ by only $\sim$ 0.02%. Thus, the impact of the approximations on the properties of the cold, equilibrium stars is negligible.

Figure A2 shows the EoS at two finite-temperatures and fixed, non-equilibrium electron fractions. We choose temperatures of $T \simeq 10$ and 30 MeV, which are motivated by the temperatures reached in the interior of the remnant at the merger. The electron fractions are fixed to 0.1 or 0.3. We note that, because Y_e^β is a density-dependent function, fixing Y_e to a constant value is a stringent test of the model, as this requires deviations from equilibrium at essentially all densities. Indeed, the errors of the approximate model are largest in this figure for $Y_e = 0.3$ just below $\rho_{\rm sat}$. At these densities, the electron fraction of the β-equilibrium EoS is ~ 0.02; thus, a value of $Y_e = 0.3$ is very far out of equilibrium, and the errors of the approximation are accordingly larger. Such extreme out-of-equilibrium conditions are not reached in our simulations.

Additional comparisons between the full and approximate EoSs for a larger sample of models can be found in RÖP . We recreate the SFHo result here, to illustrate the general agreement between the approximate and full EoSs across a range of densities and temperatures of interest in a merger.

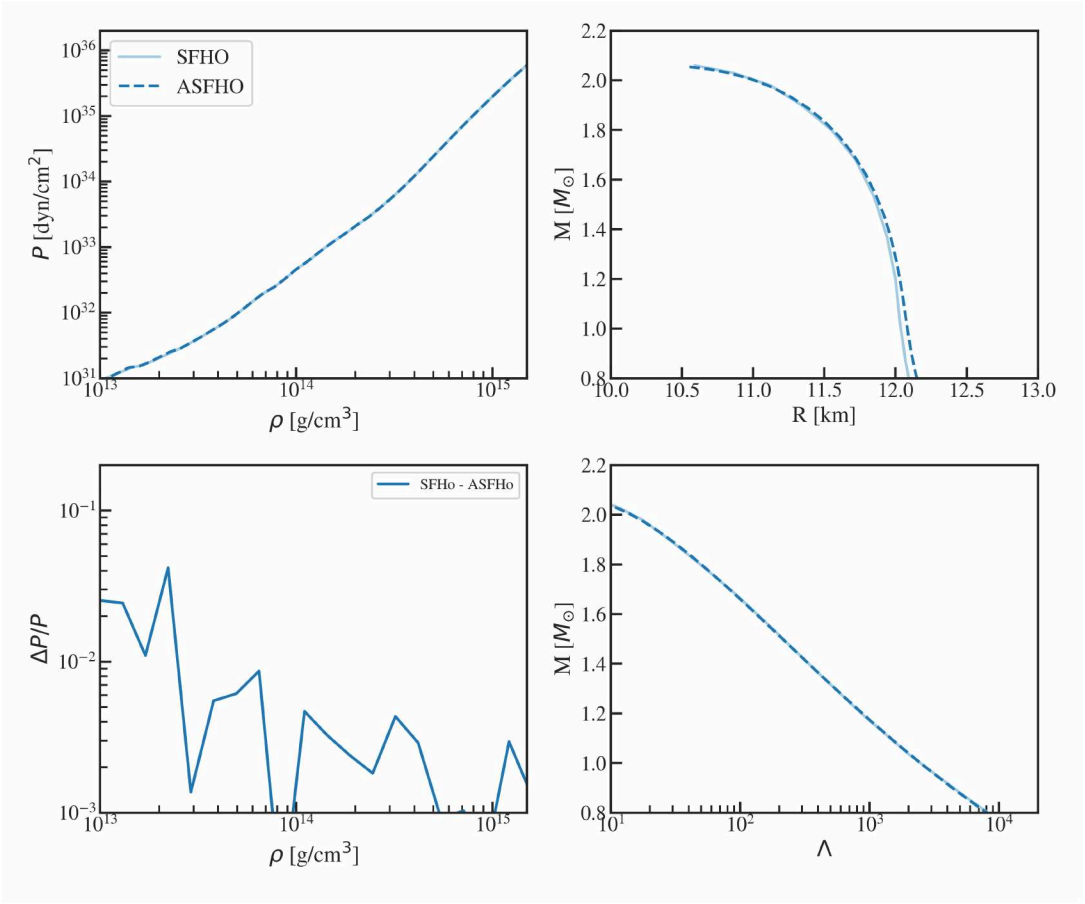

Figure A1. Clockwise from top left: the cold, β-equilibrium pressure for the full and approximate versions of SFHo; the corresponding mass-radius relations; the tidal deformability; and the fractional differences in pressure as a function of density. The solid, light-blue lines correspond to the full version of the SFHo (obtained from `stellarcollapse.org`), at $T = 0.1$ MeV and in β-equilibrium. The dashed, dark-blue lines correspond to the approximate version of SFHo under the same conditions.

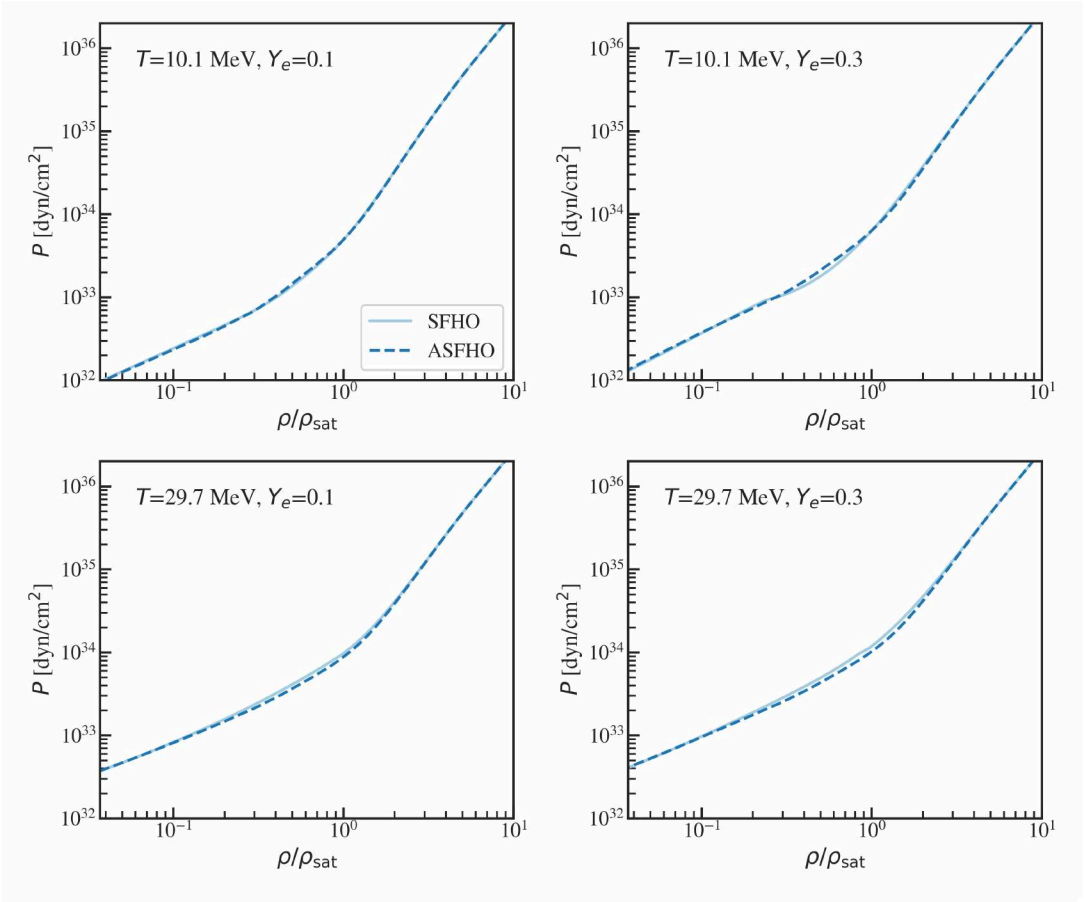

Figure A2. Comparison of the pressure model at finite temperatures and fixed electron fractions. The full version of SFHo is shown in light blue, while the approximate version is shown with the dark dashed line. The approximate EoS starts from same cold, β-equilibrium EoS and is extended to finite temperature and a fixed (non-equilibrium) electron fraction using the M^*-framework.